Original Article

Intravoxel incoherent motion diffusion-weighted imaging (IVIM-DWI) combined with conventional MRI for the detection of skull-base invasion in nasopharyngeal carcinoma: comparison with ^{18}F-sodium fluoride (^{18}F-NaF) positron emission tomography/computed tomography (PET/CT)

Yuange Li[1,2#], Qin Liu[1#], Weiquan Wu[3,4#], Zelin Liu[2], Yueling Zhang[2], Yiteng Dou[2], Qiujin Bu[2], Shuixing Zhang[1]

[1]Department of Radiology, The First Affiliated Hospital, Jinan University, Guangzhou, China; [2]Department of Radiology, Affiliated Hospital of Guangdong Medical University, Zhanjiang, China; [3]Clinical Research Experiment Center, Affiliated Hospital of Guangdong Medical University, Zhanjiang, China; [4]Faculty of Chinese Medicine, Macau University of Science and Technology, Macau, China

Contributions: (I) Conception and design: Y Li, W Wu; (II) Administrative support: S Zhang; (III) Provision of study materials or patients: Q Liu, Z Liu; (IV) Collection and assembly of data: Y Zhang, Y Dou; (V) Data analysis and interpretation: Q Bu; (VI) Manuscript writing: All authors; (VII) Final approval of manuscript: All authors.

[#]These authors contributed equally to this work.

Correspondence to: Shuixing Zhang, PhD. Department of Radiology, The First Affiliated Hospital, Jinan University, No. 613 Huangpu West Road, Tianhe District, Guangzhou 510627, China. Email: shui7515@126.com.

Background: The extent of skull base invasion (SBI) in nasopharyngeal carcinoma (NPC) directly impacts tumor staging, treatment strategies, and prognosis assessment for NPC patients, emphasizing the critical need for prompt diagnosis and precise assessment of invasion. Thus, we aimed to integrate the advantages of intravoxel incoherent motion diffusion-weighted imaging (IVIM-DWI) and conventional magnetic resonance imaging (cMRI), and assess their combined diagnostic efficacy versus that of ^{18}F-sodium fluoride (^{18}F-NaF) positron emission tomography/computed tomography (PET/CT) for detecting SBI in NPC patients.

Methods: The study prospectively and randomly recruited 62 patients newly diagnosed with NPC by pathological biopsy at the Cancer Center of Affiliated Hospital of Guangdong Medical University from January 2021 to September 2022. All patients underwent baseline cMRI, IVIM-DWI, and PET/CT scans. The IVIM-DWI analysis included 3 primary parameters: true diffusion coefficient (D), pseudodiffusion coefficient (D*), and pseudodiffusion fraction (f). SBI was defined as the involvement of any substructure confirmed by follow-up MRI and clinical symptoms. Inter-observer agreement was evaluated utilizing the intraclass correlation coefficients (ICC) and kappa coefficients. Receiver operating characteristic (ROC) curve was used to evaluate the diagnostic performance of cMRI, IVIM-DWI plus cMRI, and PET/CT. DeLong test was used to compare the areas under the curve (AUC) of the 3 modalities.

Results: Excellent inter-observer reliability was observed (range, 0.841–0.946). Among the IVIM-DWI parameters, D* + f demonstrated comparable accuracy to D + D* + f (AUC 0.906 *vs.* 0.904; sensitivity 88.9% *vs.* 89.8%; specificity 92.3% *vs.* 91.0%). IVIM-DWI plus cMRI yielded an overall AUC of 0.947, sensitivity of 92.6%, and specificity of 96.8%, surpassing cMRI alone with an AUC of 0.914 (P=0.025), sensitivity of 91.2%, and specificity of 91.7%, as well as ^{18}F-NaF PET/CT with an AUC of 0.852 (P<0.001), sensitivity of 80.1%, and specificity of 90.4%. In detecting substructures of SBI, IVIM-DWI plus cMRI showed superior

performance compared to ^{18}F-NaF PET/CT within the petrous part of the temporal bone (AUC 0.968 *vs.* 0.871, P=0.011; sensitivity 93.5% *vs.* 87.1%, specificity 100% *vs.* 87.1%), pterygopalatine fossa (AUC 0.935 *vs.* 0.831, P=0.032; sensitivity 93.9% *vs.* 69.7%, specificity 93.1% *vs.* 96.6%), and foramen ovale (AUC 0.885 *vs.* 0.710, P=0.019; sensitivity 76.9% *vs.* 61.5%, specificity 100% *vs.* 80.6%).

Conclusions: IVIM-DWI plus cMRI can accurately detect SBI and the substructures in NPC, providing a valuable reference for personalized treatment strategies and precise prognosis assessment.

Keywords: Nasopharyngeal carcinoma (NPC); skull base invasion (SBI); intravoxel incoherent motion diffusion-weighted imaging (IVIM-DWI); magnetic resonance imaging (MRI); ^{18}F-sodium fluoride positron-emission tomography/computed tomography (^{18}F-NaF PET/CT)

Submitted Apr 10, 2024. Accepted for publication Jul 11, 2024. Published online Aug 16, 2024.
doi: 10.21037/qims-24-745
View this article at: https://dx.doi.org/10.21037/qims-24-745

Introduction

Nasopharyngeal carcinoma (NPC) exhibits a significant geographic distribution, primarily concentrated in Southern China and Southeast Asia (1). Characterized by its insidious onset and initial lack of obvious clinical symptoms, NPC is often diagnosed only after it has invaded the skull (skull base invasion; SBI) and spread to cervical lymph nodes. SBI is detected in around 65.5% of NPC cases (2), and its extent directly impacts tumor staging, treatment strategies, and prognosis assessment for NPC patients, emphasizing the critical need for prompt diagnosis and precise assessment of invasion (3-5).

Pathological biopsy remains the primary method for diagnosing SBI in NPC. However, acquiring tissue samples from this region poses challenges due to its anatomical complexity. Therefore, various imaging techniques have been employed to overcome this limitation. Presently, positron emission tomography/computed tomography (PET/CT) and conventional magnetic resonance imaging (cMRI) are the established imaging techniques (6). PET/CT serves as a common screening tool for tumors and enables the identification of lesion location and extent through functional imaging. The commonly used tracers for PET/CT include ^{18}F-fluorodeoxyglucose (^{18}F-FDG) and ^{18}F-sodium fluoride (^{18}F-NaF). Previous evidence indicates that ^{18}F-NaF PET/CT has superior capability in assessing SBI involvement (SBI) in NPC and detecting more osseous metastases compared to ^{18}F-FDG PET/CT(7). Conversely, ^{18}F-FDG PET/CT exhibits better performance in node (N) and metastasis (M) staging in NPC (8). Furthermore, several studies have suggested that ^{18}F-NaF PET/CT has potential advantages in tumor (T) staging of NPC (9) and offers superior diagnostic accuracy compared to MRI in diagnosing SBI (10). However, the radioactive nature and high cost of ^{18}F-NaF PET/CT hampers its routine use (11). Meanwhile, MRI, with its high resolution and non-radiation advantages, is highly favored by clinicians as the primary imaging modality for diagnosing and monitoring SBI in NPC.

Advancements in MRI technology have introduced several functional MRI sequences alongside cMRI, including dynamic contrast-enhanced MRI (DCE-MRI), conventional diffusion-weighted imaging (DWI), and intravoxel incoherent motion DWI (IVIM-DWI). Although DCE-MRI is frequently utilized for staging and diagnosing NPC, it not only requires the administration of contrast agents and multiple scanning phases but also can only obtain relevant parameters of blood perfusion (12). Conventional DWI offers a quantitative analysis of water molecule movement in tissues but is limited to a single parameter, the apparent diffusion coefficient (ADC) (13). IVIM-DWI serves as a novel extension sequence derived from traditional DWI that does not require contrast enhancement. In IVIM-DWI, 3 parameters, including D, D*, and f, are obtained using a multi-b value bi-exponential model to capture diffusion and blood perfusion data within the tissue, which can more sensitively distinguish benign and malignant tumors (14). IVIM-DWI has shown significance in NPC staging and prognostic evaluation (15,16). Moreover, a previous study highlighted the stability and repeatability of IVIM-DWI in diagnosing SBI, especially when utilizing a substantial proportion of b values below 200 s/mm^2 (17). Thus, we aimed to integrate the advantages of cMRI and IVIM-DWI and assess their combined diagnostic efficacy against ^{18}F-NaF PET/CT in

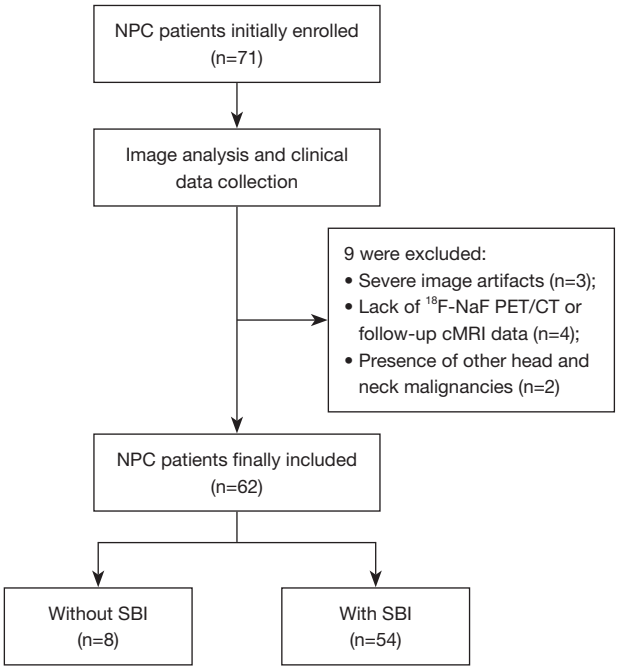

Figure 1 Study enrollment flowchart. NPC, nasopharyngeal carcinoma; ^{18}F-NaF, ^{18}F-sodium fluoride; PET/CT, positron emission tomography/computed tomography; cMRI, conventional magnetic resonance imaging; SBI, skull base invasion.

identifying SBI in NPC patients. We present this article in accordance with the STARD reporting checklist (available at https://qims.amegroups.com/article/view/10.21037/qims-24-745/rc).

Methods

Patients

The study was conducted in accordance with the Declaration of Helsinki (as revised in 2013). The prospective study received approval from the Ethics Committee of Affiliated Hospital of Guangdong Medical University (No. PJ2020-005KT), and all participants provided informed consent prior to inclusion in the study. Initially, 71 patients recently diagnosed with NPC by pathological biopsy at the Cancer Center of Affiliated Hospital of Guangdong Medical University between January 2021 and September 2022 were randomly recruited. All patients underwent cMRI, IVIM-DWI, and ^{18}F-NaF PET/CT before treatment. The time interval between pathological biopsy and various imaging examinations, as well as between MRI and ^{18}F-NaF PET/CT, did not exceed 14 days. The inclusion criteria were as follows: (I) patients diagnosed with NPC confirmed by pathological diagnosis. (II) Newly diagnosed patients who have not undergone any prior treatment. (III) Patients are required to undergo pre-treatment evaluation including routine MRI sequences of the nasopharynx and neck, IVIM-DWI sequence scans, and whole-body ^{18}F-NaF PET-CT scan, and undergo routine MRI follow-up within 3–6 months after treatment. The exclusion criteria were as follows: (I) History of other tumors in different locations or autoimmune diseases. (II) Incomplete clinical data or lack of follow-up. (III) Incomplete imaging data or poor image quality that hinders lesion assessment. Ultimately, the study excluded 9 patients due to severe image artifacts (n=3), lack of baseline PET/CT or follow-up MRI data (n=4), or current or previous malignancies other than NPC (n=2) (*Figure 1*).

MRI and PET/CT image acquisition protocols

MRI scans were conducted utilizing a GE 1.5T MRI (GE Healthcare Life Sciences, Piscataway, NJ, USA) with an 8-channel phased array head and neck coil. Patients were positioned supine with their hands resting at their sides and were advised to avoid swallowing.

The scanning coverage on the transverse axis ranged from the top border of the auricle to the bottom margin of the third cervical vertebra. In the coronal and sagittal planes, imaging included the bilateral supraclavicular fossae. The cMRI protocol comprised short time inversion recovery (STIR) and T1-weighted imaging (T1WI), sagittal T1WI, conventional DWI, as well as contrast-enhanced T1WI with fat saturation (CE-T1WI-FS) sequences across transverse axial, coronal, and sagittal planes. The IVIM-DWI data were captured utilizing a spin-echo diffusion-weighted echo-planar imaging (SE-DW-EPI) sequence. Key imaging parameters were set as follows: a 24-cm field of view, a slice thickness of 5 mm with a 1 mm slice gap, 4,000-millisecond repetition time (TR), 95-millisecond echo time (TE), 128×128 matrix, and number of excitations (NEX) =4. To reduce susceptibility artifacts, a local shim box was positioned to encompass the nasopharyngeal region. As recommended in a previous study (17), the IVIM-DWI sequence employed 9 different b values: 0, 10, 30, 50, 100, 150, 200, 600, and 1,000 s/mm^2. IVIM-DWI sequence scanning takes 2.5 minutes and post-processing takes 1.5 minutes, completing the process in a total of 4 minutes. A dose of 0.1 mmol/kg of gadolinium diethylene triamine penta-acetic acid Gd-DTPA (was) administered

intravenously to enhance contrast.

^{18}F-NaF PET/CT scanning was performed following the protocols outlined by the guidelines of the Society of Nuclear Medicine and Molecular Imaging and the European Association of Nuclear Medicine (18,19). The patients were then given an intravenous injection of ^{18}F-NaF (with radiochemical purity exceeding 95%) at a 4.07 MBq/kg dosage. Following a 1-hour rest, whole-body imaging was performed utilizing a GE Discovery 690 Elite PET/CT scanner (GE Healthcare Life Sciences, USA). Initially, a CT scan was performed utilizing automatic tube current modulation ranging from 30 to 210 mA, a noise index set at 25, and a slice thickness of 3.25 mm. Subsequently, PET scanning was carried out using the 3-dimensional (3D) mode, time-of-flight, and point-spread function acquisition and reconstruction technologies. Each patient was scanned for 1.5 minutes per bed. Attenuation correction and iterative reconstruction were performed based on the CT data to obtain whole-body images. The PET Volume Computer Assisted Reading (PET VCAR; GE Healthcare, USA) software of the workstation was employed to fuse the images and delineate regions of interest (ROIs).

Quantitative image analysis

IVIM-DWI images were analyzed on a GE Healthcare post-processing workstation using MADC software (GE Healthcare Life Sciences, USA). Maps of the IVIM-DWI quantitative parameters (D, D*, and f) were generated by selecting images with various b values for each patient to compute the bi-exponential model. Next, the maps were used to delineate the ROIs within the skull-base muscles and bones, in combination with cMRI sequences, to derive the values of D, D*, and f. The ROIs had an elliptical shape with an area of about 1.0 cm^2. Each ROI for the anatomical structure was delineated 3 times and averaged, with care taken to exclude surrounding large blood vessels. The cut-off values for SBI at each site were determined based on a previous study (17): at the base of the sphenoid bone-pterygoid process, sellar floor, and clivus, the cutoff values for D, D*, and f were 1.09×10^{-3}, 117.83×10^{-3} mm^2/s, and 0.23, respectively. In the pars petrosa of the temporal bone, the cutoff values for D, D*, and f were 2.19×10^{-3}, 132.53×10^{-3} mm^2/s, and 0.277, respectively. In the pterygopalatine fossa, the cutoff values for D, D*, and f were 1.38×10^{-3}, 108.2×10^{-3} mm^2/s, and 0.251, respectively. In the foramen oval, the cutoff values for D, D*, and f were 1.736×10^{-3}, 90.07×10^{-3} mm^2/s, and 0.241, respectively.

The diagnostic criteria for SBI with cMRI included the following: (I) a visible low signal intensity area in the bone cortex, accompanied by a change from high to low signal intensity in the marrow on T1-weighted images; (II) increased signal intensity in the skull-base muscle on STIR sequences, with the indistinct boundary between the muscle and the tumor; and (III) uneven and obvious enhancement was observed in the invaded regions of the skull base (20).

Furthermore, ^{18}F-NaF PET/CT images were presented using a hot-metal scale, where areas of high tracer uptake were depicted as bright regions, whereas low or absent tracer uptake was characterized by dark regions (21). Conversely, CT images were analyzed utilizing a bone window. The detection of regions with locally elevated or reduced tracer uptake suggested the presence of SBI.

The cMRI and IVIM-DWI images were independently and double-blindly evaluated by two radiology specialists, each with 15 years of experience. In the event of any discrepancy between the 2, they would then consult a third, more senior radiologist. These 3 radiologists were blinded to clinical details, prior investigation results, and the findings from the ^{18}F-NaF PET/CT images in this study. Additionally, the ^{18}F-NaF PET/CT images were independently and double-blindly analyzed by 2 nuclear medicine specialists, each with 15 years of experience. In the event of any discrepancy between the 2 specialists, they would consult a third, more senior nuclear medicine specialist. These 3 nuclear medicine specialists conducted the analysis without access to clinical details, previous investigation results, or the findings from the cMRI and IVIM-DWI examinations in this study.

Standard of reference for the SBI

Although pathological biopsy serves as the gold standard for diagnosing SBI, obtaining a biopsy is challenging, given the complex and deep location of the skull base. Therefore, the identification of SBI in NPC was based on the follow-up cMRI scans for up to 6 months, together with clinical symptoms. Since false positives were often seen in ^{18}F-NaF PET/CT after radiotherapy, ^{18}F-NaF PET/CT was not used for follow-up imaging (22). Positive criteria for SBI were as follows: (I) initial examinations consistently indicated SBI; (II) follow-up MRI images showed no change in the location and extent of SBI; (III) follow-up MRI images revealed an increase in the extent of SBI; (IV) follow-up MRI images showed a decrease in the extent of SBI, but the patient exhibited symptoms of basal cranial nerve invasion. Patients meeting criterion (I) combined with any of

criteria (II) through (IV) were diagnosed with SBI in NPC.

Potential sites of SBI include the base of the sphenoid bone, pterygoid process, sellar floor, clivus, petrous part of the temporal bone, pterygopalatine fossa, infratemporal fossa, foramen ovale, lacerum, sinus cavernous, and the jugular vein area (23). To ensure the presence of SBI, invasion in 1 or more of the aforementioned sites should be detected. However, to enhance the precision of the analysis, the foramen lacerum, sinus cavernosus, and jugular vein areas were excluded from the analysis due to their vascular nature. To facilitate measurements, the remaining sites were categorized into 7 distinct areas: base of the sphenoid bone-pterygoid process, sellar floor, clivus, the petrous part of the temporal bone, pterygopalatine fossa, foramen ovale, and infratemporal fossa.

Sample size evaluation

The training and validation cohorts required a sample size of at least 19 cases, considering the following inputs and assumptions: power of 95%, 2-sided significance level of 0.05, an alternative hypothesis area under the curve (AUC) of 0.900 compared to a null hypothesis AUC of 0.500, and an allocation ratio of sample sizes between negative and positive groups of 3:7. Therefore, a sample size of 19 was deemed adequate to detect an AUC difference of 0.500 with 95% power if the true AUC exceeded 0.900.

Statistical analysis

Statistical analyses were conducted utilizing SPSS 26.0 software (IBM Corp., Armonk, NY, USA) and MedCalc (version 19.6.3; MedCalc Software, Ostend, Belgium). The consistency of IVIM-DWI parameter measurements made by 3 radiologists was calculated utilizing intraclass correlation coefficient (ICC) analysis, whereas the agreement of 3 readings for cMRI and ^{18}F-NaF PET/CT were assessed using Cohen's Kappa analysis. MedCalc software was used to perform DeLong test to generate receiver operating characteristic (ROC) curves for cMRI, IVIM-DWI plus cMRI, and PET/CT, calculating AUC to evaluate diagnostic performance. A 2-tailed P value less than 0.05 was considered statistically significant.

Results

Patient characteristics

Patient inclusion is summarized in *Figure 1*. The study finally comprised 62 individuals, with 49 males and 13 females. The patients had a median age of 54 years, spanning from 30 to 77 years. Totals of 2 (3.2%), 6 (9.7%), 21 (33.9%), and 33 (53.2%) patients were at stage I to IV, respectively. Among the patients, 8 cases showed no SBI, including 3 (4.8%) at the T1 stage and 5 (8.1%) at the T2 stage; 54 cases showed SBI, with 33 (53.2%) cases at the T3 stage and 21 (33.9%) cases at the T4 stage (*Table 1*). TNM staging was determined according to the 8th edition of the American Joint Committee on Cancer/Union for International Cancer Control (AJCC/UICC) staging system for NPC (24).

A total of 434 sites on the skull base were analyzed, and 220 (50.7%) were found to be invaded. The specific sites included the sphenoid bone-pterygoid process in 53 cases (24.1%), the sellar floor in 29 cases (13.2%), the clivus base in 44 cases (20.0%), the petrous part of the temporal bone in 31 cases (14.1%), the pterygopalatine fossa in 33 cases (15.0%), the foramen ovale in 26 cases (11.8%), and the infratemporal fossa in 4 cases (1.8%). Due to the limited number of cases involving the infratemporal fossa, it was excluded from subsequent analysis, resulting in a final analysis of 372 skull base sites. *Figure 2* demonstrates the consistent diagnosis of SBI in a 35-year-old male with NPC using IVIM-DWI, cMRI, and ^{18}F-NaF PET/CT.

Inter-reader consistency

ICC and Cohen's Kappa analyses indicated good consistency (coefficients of 0.841–0.940) in the results obtained from IVIM-DWI, cMRI, and ^{18}F-NaF PET/CT measurements or analyses conducted by 2 radiologists (*Table 2*).

Diagnostic performance of the IVIM-DWI parameters

Among the single IVIM-DWI parameter, the f yielded higher precision [AUC =0.887, 95% confidence interval (CI): 0.850–0.917, sensitivity 78.7%, specificity 98.7%] than D* (AUC =0.707, 95% CI: 0.658–0.753, P<0.001; sensitivity 67.1%, specificity 74.4%) and D (AUC =0.586, 95% CI: 0.534–0.636, P<0.001; sensitivity 45.4%, specificity 71.8%). After combining these parameters, the D* + f demonstrated the greatest precision with an AUC of 0.906 (95% CI: 0.872–0.934), which showed comparable results to D + D* + f (0.904, 95% CI: 0.870–0.932, P=0.879). Moreover, the sensitivity (88.9% *vs.* 89.8%) and specificity (92.3% *vs.* 91.0%) were also similar between D* + f and D + D* + f. The addition of D to D* and f failed to produce incremental information (*Table 3*, *Figure 3A*).

Table 1 The clinical characteristics of the recruited NPC patients

Characteristics	Value
Sex	
Male	49 (79.0)
Female	13 (21.0)
Age (years), median (range)	54 (30–77)
Clinical symptoms and signs	
Epistaxis	37 (58.7)
Hearing impairment	27 (43.5)
Nasal obstruction	24 (38.7)
Headache	22 (35.5)
Facial numbness	7 (11.3)
Diplopia and eye symptoms	8 (12.9)
Cervical lymph nodes	33 (53.2)
Histopathology	
Nonkeratinizing carcinoma	61 (98.4)
Keratinizing carcinoma	1 (1.6)
TNM stage	
I	2 (3.2)
II	6 (9.7)
III	21 (33.9)
IV	33 (53.2)
T stage	
T1	3 (4.8)
T2	5 (8.1)
T3	33 (53.2)
T4	21 (33.9)
N stage	
N0	9 (14.5)
N1	21 (33.9)
N2	17 (27.4)
N3	15 (24.2)
M stage	
M0	58 (93.5)
M1	4 (6.5)

Data are represented as number (%) or median (range). NPC, nasopharyngeal carcinoma; TNM, tumor-node-metastasis.

Comparison of IVIM-DWI plus cMRI, cMRI, and PET/CT

IVIM-DWI plus cMRI achieved the highest AUC, sensitivity, and specificity, which demonstrated optimal diagnostic precision (AUC =0.947, 95% CI: 0.919–0.967, sensitivity 92.6%, specificity 96.8%). This was followed by cMRI with an AUC of 0.914 (95% CI: 0.881–0.941), sensitivity of 91.2%, and specificity of 91.7%, and ^{18}F-NaF PET/CT with an AUC of 0.852 (95% CI: 0.812–0.887), sensitivity of 80.1%, and specificity of 90.4% (*Table 4*, *Figure 3B*). The combination of IVIM-DWI with cMRI showed superior accuracy compared to ^{18}F-NaF PET/CT in detecting SBI in specific areas such as the pars petrosa of the temporal bone (AUC =0.968 *vs.* 0.871, 95% CI: 0.888–0.996 *vs.* 0.761–0.943, P=0.011; sensitivity 93.5% *vs.* 87.1%, specificity 100% *vs.* 87.1%), pterygopalatine fossa (AUC =0.935 *vs.* 0.831, 95% CI: 0.843–0.982 *vs.* 0.715–0.914, P=0.032; sensitivity 93.9% *vs.* 69.7%, specificity 93.1% *vs.* 96.6%), and foramen ovale (AUC =0.885 *vs.* 0.710, 95% CI: 0.778–0.952 *vs.* 0.581–0.819, P=0.019; sensitivity 76.9% *vs.* 61.5%, specificity 100% *vs.* 80.6%) (*Table 5*, *Figure 3C-3E*). However, it showed similar accuracy to ^{18}F-NaF PET/CT in detecting SBI in the sphenoid bone-pterygoid process (AUC =0.972 *vs.* 0.953, 95% CI: 0.894–0.997 *vs.* 0.867–0.990, P=0.416; sensitivity 94.3% *vs.* 90.6%, specificity 100% *vs.* 100%), sellar floor (AUC =0.948 *vs.* 0.914, 95% CI: 0.860–0.988 *vs.* 0.815–0.970, P=0.317; sensitivity 89.7% *vs.* 82.8%, specificity 100% *vs.* 100%), and clivus (AUC =0.917 *vs.* 0.814, 95% CI: 0.818–0.972 *vs.* 0.695–0.902, P=0.181; sensitivity 100% *vs.* 79.5%, specificity 83.3% *vs.* 83.3%) (*Table 5*, *Figure 3F-3H*). Specifically, the IVIM-DWI plus cMRI showed AUCs >0.900 in cases of invasion in all locations except for foramen ovale (AUC =0.885) (*Table 5*). Notably, the specificity of IVIM-DWI plus cMRI in diagnosing SBI in the sphenoid bone-pterygoid process, sellar floor, the petrous part of the temporal bone, and foramen ovale reached 100% (*Table 5*).

Discussion

IVIM-DWI, a novel functional imaging sequence in MRI, enables the quantitative assessment of water molecule diffusion within lesions and the perfusion of capillary microcirculation simultaneously. Over the years, many researchers have employed IVIM-DWI to diagnose and prognose various diseases across different body regions

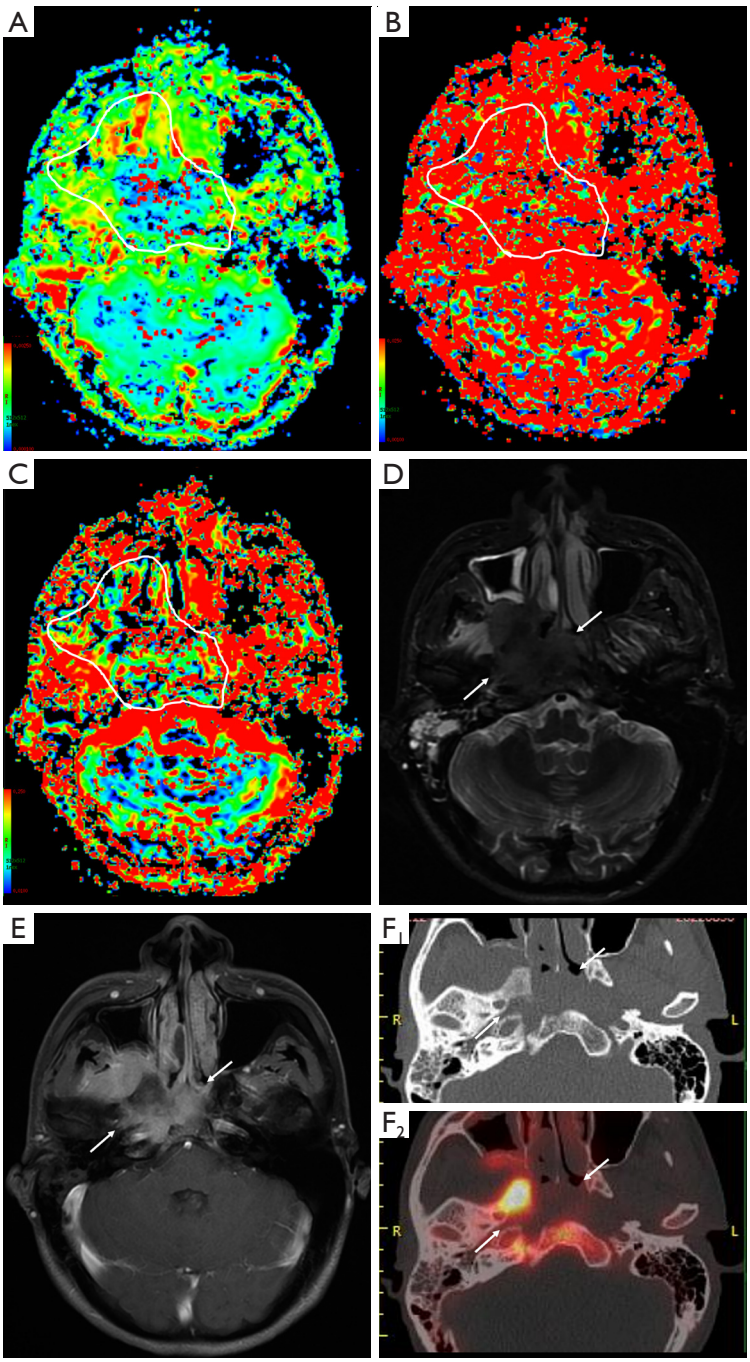

Figure 2 The consistent diagnosis of skull base invasion in a 35-year-old male with NPC using IVIM-DWI, cMRI, and PET/CT. The white circles in images (A-C) and the white arrows in images (D-F) indicate the involvement of the sphenoid bone-pterygoid process, clivus, pars petrosa of the right temporal bone, right pterygopalatine fossa, and parapharyngeal muscles. The values of D (A), D* (B), and f (C), which are derived from IVIM-DWI, decreased. The cMRI sequences showed slight hyperintensity in STIR (D) and significant CE-T1WI (E) enhancement. Additionally, CT images (F_1) in a bone window revealed localized osteolytic destruction, and PET images (F_2) showed enhanced tracer uptake. R, right; L, left; NPC, nasopharyngeal carcinoma; IVIM-DWI, intravoxel incoherent motion-diffusion weighted imaging; cMRI, conventional magnetic resonance imaging; PET/CT, positron emission tomography/computed tomography; D, pure diffusion coefficient; D*, pseudo-diffusion coefficient; f, perfusion volume fraction; STIR, short-tau inversion recovery; CE-T1WI, contrast-enhanced T1-weighted imaging; CT, computed tomography; PET, positron emission tomography.

(25-29). Moreover, it has been utilized for staging, distinguishing between different conditions, and assessing prognosis in NPC (14,30,31). However, the use of IVIM-DWI in diagnosing SBI of NPC remains limited. A previous study demonstrated the high stability and repeatability of the IVIM-DWI sequence in diagnosing SBI of NPC (17). Subsequently, IVIM-DWI images of NPC patients with SBI were subjected to post-processing and measured twice, producing satisfactory ICC values and further corroborating the findings. Building on these observations, this research evaluated the efficacy of combining the IVIM-DWI sequence with cMRI in diagnosing SBI of NPC and detecting sub-categorization of SBI compared with ^{18}F-NaF PET/CT scanning. In this study, our findings revealed that IVIM-DWI plus cMRI achieved the optimal diagnostic precision (AUC =0.947, 95% CI: 0.919–0.967), surpassing cMRI alone (AUC =0.914, 95% CI: 0.881–0.941, P=0.025) in diagnosing SBI of NPC, and outperforming ^{18}F-NaF PET/CT (AUC =0.852, 95% CI: 0.812–0.887, P<0.001). There was no significant difference between cMRI and ^{18}F-NaF PET/CT in the diagnosis of various parts of SBI of NPC, consistent with previous evidence (9). However, the combination of IVIM-DWI with cMRI exhibited superior accuracy compared to 18F-NaF PET/CT in detecting SBI in specific areas such as the pars petrosa of the temporal bone (P=0.011), pterygopalatine fossa (P=0.032), and foramen ovale (P=0.019). This suggests clinical significance in our study.

IVIM-DWI employs a multi-b-value double exponential model to distinguish tissue diffusion and perfusion information, yielding 3 parameters (D, D*, f). Previous studies (32-35) have shown that the resulting AUC value tends to be low when using a single parameter alone for disease diagnosis or prognosis evaluation. Our previous study (17) and the present study have yielded similar findings. However, when the 3 parameters are integrated in varying combinations, the AUC value improves to different extents. Nevertheless, the combination that exhibits the highest diagnostic efficiency has yet to be determined. In the current study, we performed a comparative analysis of different combinations of IVIM-DWI parameters. The results demonstrated that the combined application of D* + f and D + D* + f exhibited the highest diagnostic efficacy for detecting SBI of NPC.

The discriminative capabilities of cMRI, IVIM-DWI plus cMRI, and ^{18}F-NaF PET/CT were evaluated utilizing the AUC value. The findings revealed that the IVIM-DWI plus cMRI exhibited a higher diagnostic performance than

Table 2 The intra-observer consistency of IVIM-DWI, cMRI, and ^{18}F-NaF PET/CT measured and analyzed by 2 radiologists

Modalities	ICC or Kappa value (95% CI)	P value
IVIM-DWI		
D	0.927 (0.911–0.940)	<0.001
D*	0.946 (0.935–0.956)	<0.001
f	0.912 (0.893–0.928)	<0.001
cMRI	0.935 (0.921–0.947)	<0.001
^{18}F-NaF PET/CT	0.841 (0.809–0.868)	<0.001

IVIM-DWI, intravoxel incoherent motion diffusion-weighted imaging; cMRI, conventional magnetic resonance imaging; ^{18}F-NaF PET/CT, ^{18}F-sodium fluoride positron emission tomography/computed tomography; ICC, intraclass correlation coefficient; CI, confidence interval; D, true diffusion coefficient; D*, pseudodiffusion coefficient; f, pseudodiffusion fraction.

Table 3 The diagnostic performance of IVIM-DWI parameters for SBI

Parameters	AUC (95% CI)	Sensitivity (95% CI)	Specificity (95% CI)
D	0.586 (0.534–0.636)	45.4 (38.6–52.3)	71.8 (64.0–78.7)
D*	0.707 (0.658–0.753)	67.1 (60.4–73.4)	74.4 (66.8–81.0)
f	0.887 (0.850–0.917)	78.7 (72.6–84.0)	98.7 (95.4–99.8)
D + D*	0.738 (0.690–0.782)	88.0 (82.9–92.0)	59.6 (51.5–67.4)
D + f	0.893 (0.857–0.922)	87.5 (82.3–91.6)	91.0 (85.4–95.0)
D* + f	0.906 (0.872–0.934)	88.9 (83.9–92.7)	92.3 (86.9–96.0)
D + D* + f	0.904 (0.870–0.932)	89.8 (85.0–93.5)	91.0 (85.4–95.0)

IVIM-DWI, intravoxel incoherent motion diffusion-weighted imaging; SBI, skull base invasion; AUC, area under the curve; CI, confidence interval; D, true diffusion coefficient; D*, pseudodiffusion coefficient; f, pseudodiffusion fraction.

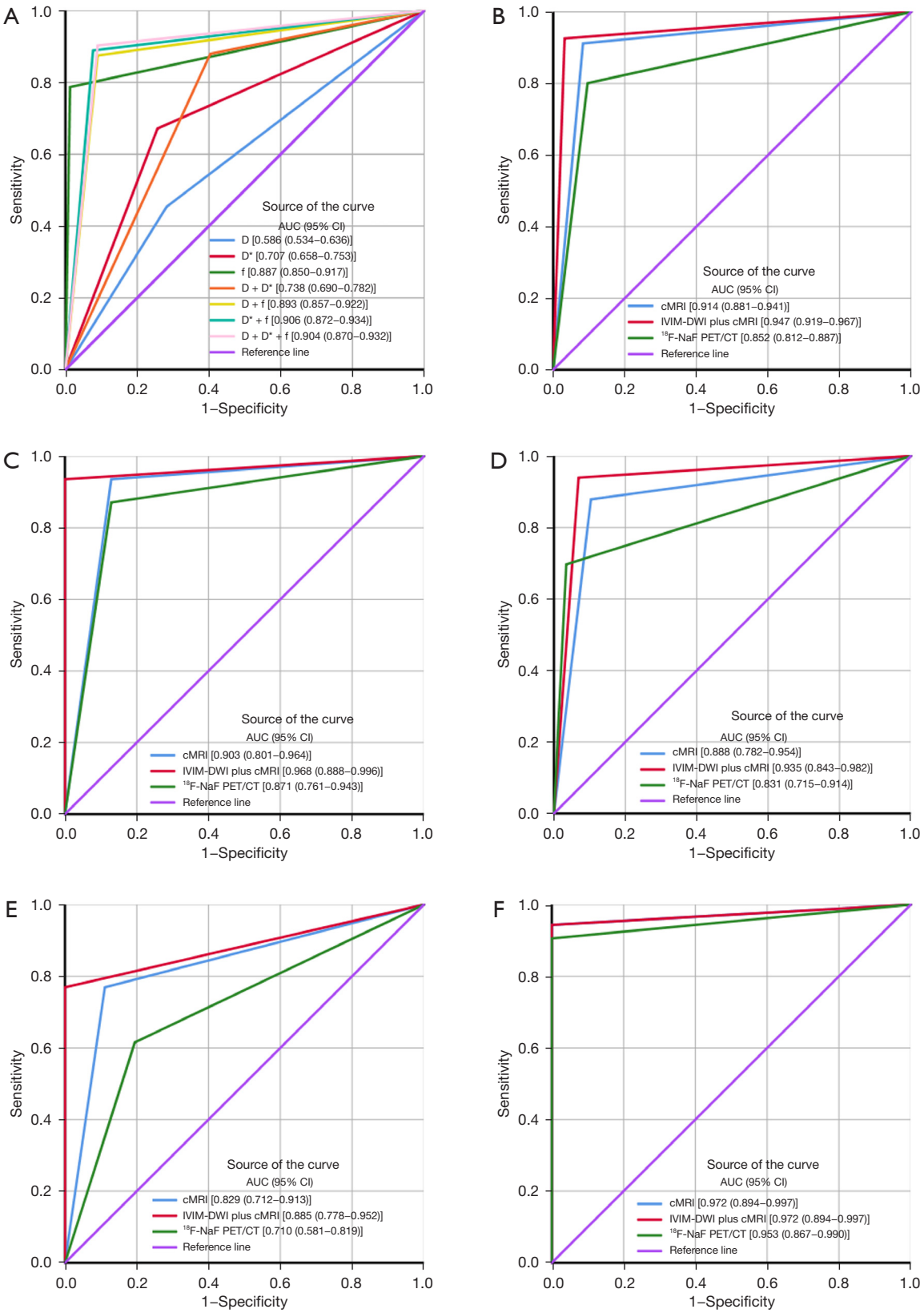

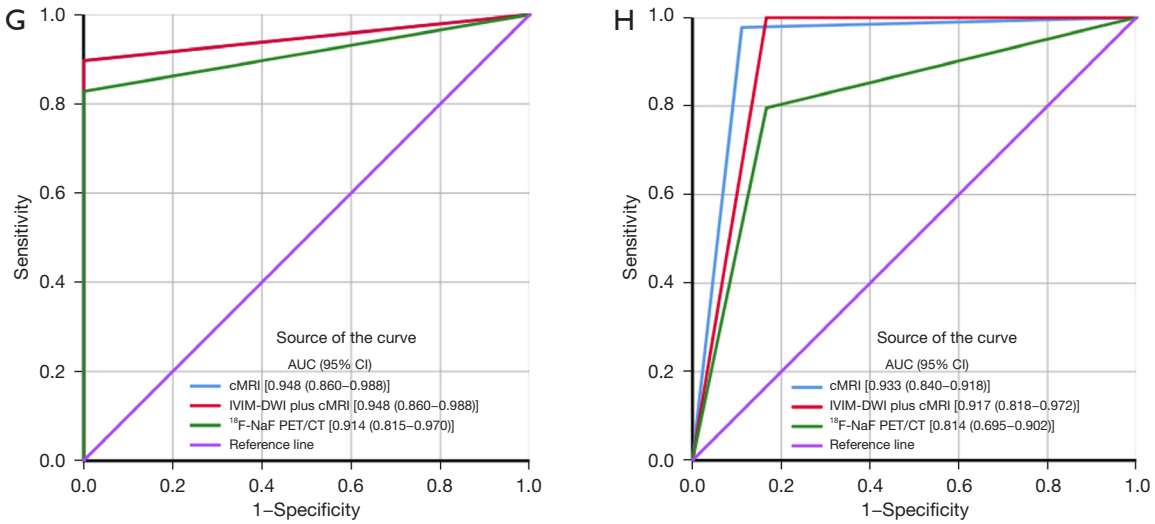

Figure 3 ROC curves of IVIM-DWI, cMRI, and PET/CT in the detection of SBI in NPC patients. Comparisons were conducted to evaluate the effectiveness of IVIM-DWI parameters in detecting various subsites of SBI (A). Additionally, the performance of IVIM-DWI plus cMRI, cMRI, and PET/CT were compared in detecting any subsite of SBI (B), as well as specific subsites, including the sphenoid bone-pterygoid process (C), sellar floor (D), clivus (E), pars petrosa of the temporal bone (F), pterygopalatine fossa (G), and foramen ovale (H). D, pure diffusion coefficient; AUC, area under the curve; D*, pseudo-diffusion coefficient; f, perfusion volume fraction; cMRI, conventional magnetic resonance imaging; IVIM-DWI, intravoxel incoherent motion-diffusion weighted imaging; ^{18}F-NaF PET/CT, ^{18}F-sodium fluoride positron emission tomography/computed tomography; ROC, receiver operating characteristic; SBI, skull base invasion; NPC, nasopharyngeal carcinoma.

Table 4 The diagnostic performance of cMRI, IVIM-DWI plus cMRI, and ^{18}F-NaF PET/CT in detecting SBI of NPC

Modalities	AUC (95% CI)	P value	Sensitivity (95% CI), %	Specificity (95% CI), %
cMRI	0.914 (0.881–0.941)	0.025	91.2 (86.6–94.6)	91.7 (86.2–95.5)
IVIM-DWI plus cMRI	0.947 (0.919–0.967)	Ref	92.6 (88.2–95.7)	96.8 (92.7–99.0)
^{18}F-NaF PET/CT	0.852 (0.812–0.887)	<0.001	80.1 (74.1–85.2)	90.4 (84.6–94.5)

Ref represents reference value. cMRI, conventional magnetic resonance imaging; IVIM-DWI, intravoxel incoherent motion diffusion-weighted imaging; ^{18}F-NaF PET/CT, ^{18}F-sodium fluoride positron emission tomography/computed tomography; SBI, skull base invasion; NPC, nasopharyngeal carcinoma; AUC, area under the curve; CI, confidence interval.

^{18}F-NaF PET/CT. This observation could be attributed to 2 main factors. First, IVIM-DWI allowed for quantitative assessment of lesions, although with lower image resolution. Conversely, cMRI provided high-resolution images. Thus, the IVIM-DWI plus cMRI was considered mutually complementary. Second, some studies indicate that ^{18}F-NaF PET/CT demonstrates high specificity in diagnosing skull base bone invasion (SBBI), yet it exhibits lower accuracy than cMRI in visualizing soft tissue involvement in NPC (9,10).

In recent years, many researchers have proposed the subclassification of SBI of NPC into slight SBI (invasion of pterygoid processes and base of sphenoid bone) and severe SBI (other SBIs) as it facilitates precise selection of treatment options and assessment of prognosis (36). cMRI is commonly employed for diagnosing and assessing the prognosis of SBI in NPC. Therefore, it is considered a reliable method capable of accurately distinguishing different subtypes of SBI of NPC and serving as an independent factor in prognosis evaluation (20). These findings align with the results obtained in this study. Moreover, the study results indicated that cMRI exhibited superior diagnostic efficacy in several locations of SBI of NPC. Particularly, when combined with IVIM-DWI, the diagnostic efficacy for SBI of NPC in the petrous part of

Table 5 The diagnostic performance of cMRI, IVIM-DWI plus cMRI, and ^{18}F-NaF PET/CT in detecting the substructures of SBI

Subsites	Modalities	AUC (95% CI)	P value	Sensitivity (95% CI), %	Specificity (95% CI), %
Pars petrosa of the temporal bone	cMRI	0.903 (0.801–0.964)	0.483	93.5 (78.6–99.2)	87.1 (70.2–96.4)
	IVIM-DWI plus cMRI	0.968 (0.888–0.996)	0.011	93.5 (78.6–99.2)	100 (88.8–100)
	^{18}F-NaF PET/CT	0.871 (0.761–0.943)	Ref	87.1 (70.2–96.4)	87.1 (70.2–96.4)
Pterygopalatine fossa	cMRI	0.888 (0.782–0.954)	0.326	87.9 (71.8–96.6)	89.7 (72.6–97.8)
	IVIM-DWI plus cMRI	0.935 (0.843–0.982)	0.032	93.9 (79.8–99.3)	93.1 (77.2–99.2)
	^{18}F-NaF PET/CT	0.831 (0.715–0.914)	Ref	69.7 (51.3–84.4)	96.6 (82.2–99.9)
Foramen ovale	cMRI	0.829 (0.712–0.913)	0.105	76.9 (56.4–91.0)	88.9 (73.9–96.9)
	IVIM-DWI plus cMRI	0.885 (0.778–0.952)	0.019	76.9 (56.4–91.0)	100 (90.3–100)
	^{18}F-NaF PET/CT	0.710 (0.581–0.819)	Ref	61.5 (40.6–79.8)	80.6 (64.0–91.8)
Sphenoid bone-pterygoid process	cMRI	0.972 (0.894–0.997)	0.416	94.3 (84.3–98.8)	100 (66.4–100)
	IVIM-DWI plus cMRI	0.972 (0.894–0.997)	0.416	94.3 (84.3–98.8)	100 (66.4–100)
	^{18}F-NaF PET/CT	0.953 (0.867–0.990)	Ref	90.6 (79.3–96.9)	100 (66.4–100)
Sellar floor	cMRI	0.948 (0.860–0.988)	0.317	89.7 (72.6–97.8)	100 (89.4–100)
	IVIM-DWI plus cMRI	0.948 (0. 860–0.988)	0.317	89.7 (72.6–97.8)	100 (89.4–100)
	^{18}F-NaF PET/CT	0.914 (0.815–0.970)	Ref	82.8 (64.2–94.2)	100 (89.4–100)
Clivus	cMRI	0.933 (0.840–0918)	0.100	97.7 (88.0–99.9)	88.9 (65.3–98.6)
	IVIM-DWI plus cMRI	0.917 (0.818–0.972)	0.181	100 (92.0–100)	83.3 (58.6–96.4)
	^{18}F-NaF PET/CT	0.814 (0.695–0.902)	Ref	79.5 (64.7–90.2)	83.3 (58.6–96.4)

Ref represents reference value. cMRI, conventional magnetic resonance imaging; IVIM-DWI, intravoxel incoherent motion diffusion-weighted imaging; ^{18}F-NaF PET/CT, ^{18}F-sodium fluoride positron emission tomography/computed tomography; SBI, skull base invasion; AUC, area under the curve; CI, confidence interval.

the temporal bone, the pterygopalatine fossa, along with the foramen ovale was further enhanced. The petrous part of the temporal bone, pterygopalatine fossa, and foramen ovale were sites commonly associated with severe SBI. This underscored that combining IVIM-DWI with cMRI enabled accurate subclassification of SBI of NPC and early identification of the extensive invasion type, thereby facilitating precise treatment planning.

One intriguing finding of this study is that the combination of IVIM-DWI with cMRI exhibited lower diagnostic accuracy than cMRI alone in diagnosing clivus invasion of NPC. The sensitivity reached 100% in this case, but the specificity was lower. The cause of this situation may be that the clivus undergoes red-yellow bone marrow conversion easily depending on the patient's physical condition, resulting in variations in fat and iron content within the clivus and consequently leading to nonspecific changes in IVIM-DWI parameters. Some researchers have already achieved similar results (37,38). For instance, a study found that older individuals with higher liver iron content paradoxically exhibited higher f and D* values compared to younger cases (37), whereas another study observed a paradoxical increase in liver f in steatotic livers (38).

The present study has some limitations. First, there is currently no established pathological gold standard for SBI, which may introduce uncertainties in the diagnostic process. Second, the sample size was relatively small, emphasizing the necessity for larger-scale studies to further validate the results. Third, the limitations of IVIM were not taken into account, such as prolonged acquisition time and non-specific alterations in IVIM-DWI parameters influenced by red-yellow bone marrow conversion. Overcoming these imitations of IVIM-DWI is our next goal, for instance, we plan to apply a DWI-derived surrogate biomarker, diffusion-derived vessel density (DDVD), to diagnose SBI in NPC.

Conclusions

The integration of IVIM-DWI and cMRI demonstrated superior diagnostic efficacy compared to ^{18}F-NaF PET/CT in cases of SBI, especially for the subclassifications involving the petrous part of the temporal bone, pterygopalatine fossa, as well as the foramen ovale. Notably, the petrous part of the temporal bone, pterygopalatine fossa, and foramen ovale were sites commonly associated with severe SBI. Overall, IVIM-DWI plus cMRI holds significant potential for accurate diagnosis of SBI and its subcategorization in NPC, thus providing a reliable basis for developing personalized treatment strategies and assessing prognosis accurately.

Acknowledgments

We would like to thank all the participants in this study.
Funding: This work was supported by the Medical Science and Technology Research Fund of Guangdong, China (Nos. A2023249 and A2023247) and the Imaging Alliance Fund Project of Southern Medical University, China (No. FS2023010019).

Footnote

Reporting Checklist: The authors have completed the STARD reporting checklist. Available at https://qims.amegroups.com/article/view/10.21037/qims-24-745/rc

Conflicts of Interest: All authors have completed the ICMJE uniform disclosure form (available at https://qims.amegroups.com/article/view/10.21037/qims-24-745/coif). The authors have no conflicts of interest to declare.

Ethical Statement: The authors are accountable for all aspects of the work in ensuring that questions related to the accuracy or integrity of any part of the work are appropriately investigated and resolved. The study was conducted in accordance with the Declaration of Helsinki (as revised in 2013). The prospective study was approved by the Ethics Committee of Affiliated Hospital of Guangdong Medical University (No. PJ2020-005KT), and informed consent was provided by all participants.

References

1. Chen YP, Chan ATC, Le QT, Blanchard P, Sun Y, Ma J. Nasopharyngeal carcinoma. Lancet 2019;394:64-80.
2. Li YZ, Cai PQ, Xie CM, Huang ZL, Zhang GY, Wu YP, Liu LZ, Lu CY, Zhong R, Wu PH. Nasopharyngeal cancer: impact of skull base invasion on patients prognosis and its potential implications on TNM staging. Eur J Radiol 2013;82:e107-11.
3. Li HJ, Hu YY, Huang L, Zhou J, Li JJ, Xie CB, Chen MY, Sun Y, Liu LZ, Tian L. Subclassification of skull-base invasion for nasopharyngeal carcinoma using cluster, network and survival analyses: A double-center retrospective investigation. Radiother Oncol 2019;134:37-43.
4. Roh JL, Sung MW, Kim KH, Choi BY, Oh SH, Rhee CS, Ha JW. Nasopharyngeal carcinoma with skull base invasion: a necessity of staging subdivision. Am J Otolaryngol 2004;25:26-32.
5. Wu B, Guo Y, Yang HH, Gao QG, Tian Y. Predicting Bone Metastasis Risk Based on Skull Base Invasion in Locally Advanced Nasopharyngeal Carcinoma. Front Oncol 2022;12:812358.
6. Gihbid A, Cherkaoui Salhi G, El Alami I, Belgadir H, Tawfiq N, Bendahou K, El Mzibri M, Cadi R, El Benna N, Guensi A, Khyatti M. Pretreatment [18F]FDG PET/CT and MRI in the prognosis of nasopharyngeal carcinoma. Ann Nucl Med 2022;36:876-86.
7. Zhang Y, Chen Y, Huang Z, Zhang L, Wan Q, Lei L. Comparison of (18)F-NaF PET/CT and (18)F-FDG PET/CT for Detection of Skull-Base Invasion and Osseous Metastases in Nasopharyngeal Carcinoma. Contrast Media Mol Imaging 2018;2018:8271313.
8. Xie HJ, Sun XS, Zhang X, Xiao BB, Lin DF, Lin XP, Lv XF, Liu LZ, Han F, Zou RH, Li JB, Fan W, Chen QY, Mai HQ, Tang LQ. Head and neck MRI-based T stage and [18F]FDG PET/CT-based N/M stage improved prognostic stratification in primary nasopharyngeal carcinoma. Eur Radiol 2023;33:7952-66.
9. Wang D, Guo C, Xiao J. The potential advantages of (18)F

sodium fluoride positron emission tomography-computed tomography for clinical staging and management planning in patients with nasopharyngeal carcinoma. Quant Imaging Med Surg 2024;14:3393-404.
10. Le Y, Chen Y, Zhou F, Liu G, Huang Z, Chen Y. Comparative diagnostic value of 18F-fluoride PET-CT versus MRI for skull-base bone invasion in nasopharyngeal carcinoma. Nucl Med Commun 2016;37:1062-8.
11. Xiao J, Wang D, Guo B, Wang L, Su M, Xu H. Observer agreement and accuracy of 18F-sodium fluoride PET/computed tomography in the diagnosis of skull-base bone invasion and osseous metastases in newly diagnosed nasopharyngeal carcinoma. Nucl Med Commun 2020;41:942-9.
12. Liu L, Hu L, Zeng Q, Peng D, Chen Z, Huang C, Liu Z, Wen Q, Zou F, Yan L. Dynamic contrast-enhanced MRI of nasopharyngeal carcinoma: correlation of quantitative dynamic contrast-enhanced magnetic resonance imaging (DCE-MRI) parameters with hypoxia-inducible factor 1α expression and tumor grade/stage. Ann Palliat Med 2021;10:2238-53.
13. Wang C, Liu L, Lai S, Su D, Liu Y, Jin G, Zhu X, Luo N. Diagnostic value of diffusion-weighted magnetic resonance imaging for local and skull base recurrence of nasopharyngeal carcinoma after radiotherapy. Medicine (Baltimore) 2018;97:e11929.
14. Ai QY, King AD, Chan JSM, Chen W, Chan KCA, Woo JKS, Zee BCY, Chan ATC, Poon DMC, Ma BBY, Hui EP, Ahuja AT, Vlantis AC, Yuan J. Distinguishing early-stage nasopharyngeal carcinoma from benign hyperplasia using intravoxel incoherent motion diffusion-weighted MRI. Eur Radiol 2019;29:5627-34.
15. Qin Y, Chen C, Chen H, Gao F. The value of intravoxel incoherent motion model-based diffusion-weighted imaging for predicting long-term outcomes in nasopharyngeal carcinoma. Front Oncol 2022;12:902819.
16. Lai V, Li X, Lee VH, Lam KO, Fong DY, Huang B, Chan Q, Khong PL. Nasopharyngeal carcinoma: comparison of diffusion and perfusion characteristics between different tumour stages using intravoxel incoherent motion MR imaging. Eur Radiol 2014;24:176-83.
17. Wu W, Xia J, Li B, Liu W, Ge Z, Tan Z, Bu Q, Chen W, Li Y. Feasibility evaluation of intravoxel incoherent motion diffusion-weighted imaging in the diagnosis of skull-base invasion in nasopharyngeal carcinoma. J Cancer 2023;14:290-8.
18. Donohoe K, Ahuja S. Society of Nuclear Medicine and Molecular Imaging Efforts Toward Standardization: From Procedure Standards to Appropriate Use Criteria. Semin Nucl Med 2019;49:153-60.
19. Geraldes FO. Annual Congress of the European Association of Nuclear Medicine 2021. Lancet Oncol 2021;22:1655.
20. Feng Y, Cao C, Hu Q, Chen X. Grading of MRI-detected skull-base invasion in nasopharyngeal carcinoma with skull-base invasion after intensity-modulated radiotherapy. Radiat Oncol 2019;14:10.
21. Wang D, Li H, Guo C, Huang S, Guo X, Xiao J. The value of (18)F-NaF PET/CT in the diagnosis of bone metastases in patients with nasopharyngeal carcinoma using visual and quantitative analyses. Front Bioeng Biotechnol 2022;10:949480.
22. Zhang SX, Han PH, Zhang GQ, Wang RH, Ge YB, Ren ZG, Li JS, Fu WH. Comparison of SPECT/CT, MRI and CT in diagnosis of skull base bone invasion in nasopharyngeal carcinoma. Biomed Mater Eng 2014;24:1117-24.
23. Han J, Zhang Q, Kong F, Gao Y. The incidence of invasion and metastasis of nasopharyngeal carcinoma at different anatomic sites in the skull base. Anat Rec (Hoboken) 2012;295:1252-9.
24. Wang Y, Zhao J, Zhao Y, Yang Z, Lei M, Li Z, Wei R, Chen D, He Y, Shen L. Impact of paranasal sinus invasion on advanced nasopharyngeal carcinoma treated with intensity-modulated radiation therapy: the validity of advanced T stage of AJCC/UICC eighth edition staging system. Cancer Med 2018;7:2826-36.
25. Yao W, Liu J, Zheng J, Lu P, Zou S, Xu Y. Study on diagnostic value of quantitative parameters of intravoxel incoherent motion diffusion-weighted imaging (IVIM-DWI) in prostate cancer. Am J Transl Res 2021;13:3696-702.
26. Chen F, Yang H, Zhu R. Analysis of IVIM DWI for the clinical diagnosis of cervical cancer. Panminerva Med 2022;64:409-10.
27. Zhou Y, Zheng J, Yang C, Peng J, Liu N, Yang L, Zhang XM. Application of intravoxel incoherent motion diffusion-weighted imaging in hepatocellular carcinoma. World J Gastroenterol 2022;28:3334-45.
28. Hu H, Jiang H, Wang S, Jiang H, Zhao S, Pan W. 3.0 T MRI IVIM-DWI for predicting the efficacy of neoadjuvant chemoradiation for locally advanced rectal cancer. Abdom Radiol (NY) 2021;46:134-43.
29. Liu B, Zeng Q, Huang J, Zhang J, Zheng Z, Liao Y, Deng K, Zhou W, Xu Y. IVIM using convolutional neural networks predicts microvascular invasion in HCC. Eur

Radiol 2022;32:7185-95.
30. Yu XP, Hou J, Li FP, Wang H, Hu PS, Bi F, Wang W. Intravoxel Incoherent Motion Diffusion Weighted Magnetic Resonance Imaging for Differentiation Between Nasopharyngeal Carcinoma and Lymphoma at the Primary Site. J Comput Assist Tomogr 2016;40:413-8.
31. Qamar S, King AD, Ai QH, So TY, Mo FKF, Chen W, Poon DMC, Tong M, Ma BB, Hui EP, Yeung DK, Wang YX, Yuan J. Pre-treatment intravoxel incoherent motion diffusion-weighted imaging predicts treatment outcome in nasopharyngeal carcinoma. Eur J Radiol 2020;129:109127.
32. Xiao Y, Chen Y, Chen Y, He Z, Yao Y, Pan J. Longitudinal Assessment of Intravoxel Incoherent Motion Diffusion Weighted Imaging in Evaluating the Radio-sensitivity of Nasopharyngeal Carcinoma Treated with Intensity-Modulated Radiation Therapy. Cancer Res Treat 2019;51:345-56.
33. Qin Y, Yu X, Hou J, Hu Y, Li F, Wen L, Lu Q, Fu Y, Liu S. Predicting chemoradiotherapy response of nasopharyngeal carcinoma using texture features based on intravoxel incoherent motion diffusion-weighted imaging. Medicine (Baltimore) 2018;97:e11676.
34. Liao L, Liu T, Wei B. Prediction of short-term treatment outcome of nasopharyngeal carcinoma based on voxel incoherent motion imaging and arterial spin labeling quantitative parameters. Eur J Radiol Open 2023;10:100466.
35. Hou J, Yu X, Hu Y, Li F, Xiang W, Wang L, Wang H, Lu Q, Zhang Z, Zeng W. Value of intravoxel incoherent motion and dynamic contrast-enhanced MRI for predicting the early and short-term responses to chemoradiotherapy in nasopharyngeal carcinoma. Medicine (Baltimore) 2016;95:e4320.
36. Li S, Luo C, Huang W, Zhu S, Ruan G, Liu L, Li H. Value of skull base invasion subclassification in nasopharyngeal carcinoma: implication for prognostic stratification and use of induction chemotherapy. Eur Radiol 2022;32:7767-77.
37. Xiao BH, Wáng YXJ. Different tissue types display different signal intensities on b = 0 images and the implications of this for intravoxel incoherent motion analysis: Examples from liver MRI. NMR Biomed 2021;34:e4522.
38. Wáng YXJ. Observed paradoxical perfusion fraction elevation in steatotic liver: An example of intravoxel incoherent motion modeling of the perfusion component constrained by the diffusion component. NMR Biomed 2021;34:e4488.

Cite this article as: Li Y, Liu Q, Wu W, Liu Z, Zhang Y, Dou Y, Bu Q, Zhang S. Intravoxel incoherent motion diffusion-weighted imaging (IVIM-DWI) combined with conventional MRI for the detection of skull-base invasion in nasopharyngeal carcinoma: comparison with ^{18}F-sodium fluoride (^{18}F-NaF) positron emission tomography/computed tomography (PET/CT). Quant Imaging Med Surg 2024;14(9):6908-6921. doi: 10.21037/qims-24-745

